[11] Matranga, G. J., Mallick, D. L., and Kluever, E. E., "An Assessment of Ground and Flight Simulators for the Examination of Manned Lunar Landing," AIAA Paper 67-238, Cocoa Beach, Fla., 1967.

[12] Hewes, D. E., "Interim Report on Flight Evaluations of Lunar Landing Vehicle Attitude Control Systems," AIAA Paper 67-239, Cocoa Beach, Fla., 1967.

[13] Hatch, H. G., Jr., Pennington, J. E., and Cobb, J. B., "Dynamic Simulation of Lunar Module Docking with Apollo Command Module in Lunar Orbit," TN D-3972, June 1967, NASA.

[14] Mimno, P., "Digital Simulation Manual," IL R-599, Jan. 1968, MIT, Cambridge, Mass.

[15] Goetzinger, J. D., "Pre-Simulation Report: LM Dynamics Simulation," IL E-2079, Sept. 1966, MIT, Cambridge, Mass.

AUGUST 1970 J. SPACECRAFT VOL. 7, NO. 8

Network Support Simulation and Sensitivities Analysis for the Saturn-Apollo Missions

WALKER H. LAND JR.*
IBM Corporation, Huntsville, Ala.

The approach is to develop, by simulation and analytical techniques, network sensitivity timeline error graphs. These graphs depict the nominal and perturbed coverage times, nominal and perturbed acquisition of signal (AOS), and loss of signal (LOS) as a function of a continuous range of trajectory errors at parking orbit insertion. The superposition principle, as used here, states that the total motion, $X(t)$, when subjected to a total error result, $F(t)$, is the sum of separate motions $X_1(t), X_2(t), \ldots X_n(t)$, arising from the individual error sources, $F_1(t), F_2(t), \ldots F_n(t)$, so long as the separate motions are contained within the linear region of the solution space. The resulting sensitivities graphs are not restricted to the parking orbit for a particular mission for the Saturn V. Another advantage is that a real-time computer solution is not required to reconfigure the network, as previously was the case. This approach has been experimentally verified by simulation and used in both the Apollo 7 and 8 missions. Also, included are the results of a post-flight data analysis of theoretical versus actual network coverage for the AS-204 and AS-501 missions. This analysis considers the effects of refractive bending of RF signals, multipath, signal dropout, and polarization diversity.

Method of Approach and Superposition Principle

THE error timeline shows the coverage time, AOS and LOS times for the nominal, and the errors from the nominal, for each of the separate trajectory variables. The abscissa of each error graph depicts the time (in seconds) from parking orbit insertion while the ordinate shows the error at parking orbit insertion in the stated trajectory variable. For no error, the resulting AOS and LOS times would be those of the nominal. Within the linear region of the AOS and LOS error curves, the total error may be obtained by the algebraic addition of the separate AOS and LOS errors.

Without some advanced knowledge of the magnitude of the errors at parking orbit insertion, a large number of timelines could possibly exist, all of which could depict the actual network. That is, there are five possible errors (excluding ascent-to-orbit time error which is not a trajectory error) in the trajectory variables at parking orbit insertion and a possibly infinite number (not infinite range) of values that these error variables may have. This means that $5X^5$ different combinations of errors (where X is a very large number) may exist a priori. For example, if X were 4, a small number indeed, 5120 timelines are required to describe all possible combinations of these errors. Using the superposition principle, this large number of required timelines is reduced to five, regardless of the size of X.

Examples of sensitivity graphs constructed using simulation techniques (in the vicinity of 5800–6500 sec for the fixed azimuth of 72° of the AS-205 mission) are depicted in Fig. 1.

These graphs are to be used as follows: a) determine the errors at parking orbit insertion from the real-time trajectory data by the methods depicted in the mathematical appendix; b) for these errors determine the change in the timeline for each error variable using Fig. 1; c) then algebraically add the separate deviations for each trajectory error in AOS and LOS to obtain the total AOS and LOS error for each station. Use these adjusted AOS and LOS times, for each station, to obtain the updated network. The variable launch azimuth case, to be described in the AS-503 sensitivity timeline error graph preparation, is handled in essentially the same manner.

AS-205 Sensitivity and Postflight Data Analysis

Simulation Validation of Superposition Principle

The superposition principle was experimentally verified using the perturbation cases 1–6 in Table 1.

Table 2, which shows the results of a portion of this analysis, was developed as follows. The AOS and LOS times were generated for each of the trajectory errors that were taken separately and also for these trajectory errors taken collectively. (Errors here mean deviations from the nominal.)

Presented as Paper 69-936 at the AIAA Aerospace Computer, Systems Conference Los Angeles, Calif., September 8–10, 1969; submitted September 22, 1970; revision received April 27, 1970. The author acknowledges A. McNair, NASA I-MO Contract Monitor; R. E. Gordon, who suggested the original problem; and N. K. Denmark, who worked with the author in the AS-204 and AS-501 data analysis. This work was done under NAS 8-14000 contract.

* Staff Engineer, Federal Systems Division.

Table 1 Perturbations at parking orbit insertion[a]

Case	δR, 10^3 m	δV, m/sec	$\delta\gamma$, deg	$\delta i = \delta \mho$, deg	Run time, sec
1	30	+50	2.0	5.5	16,192
3	+20	+20	+0.5	1.5	16,192
5	+10	+20	+1.0	+1.5	5,764

[a] Case 2 is same as case 1; except all perturbations are negative; case 4 as case 3; except all perturbations are negative; and case 6, as case 5, except delta gamma equals +2.0°.

The errors in AOS and LOS were obtained for separate cases using finite differences, algebraically added, and compared to the collective trajectory error results. Algebraic addition, rather than rms, was used because of the application of the superposition principle.

Case 1 depicts the largest positive errors considered in the trajectory variables at parking orbit insertion. The results of Table 2 (cases 1 and 4) show agreement in AOS and LOS time to within 15 sec in most cases.

The errors of case 2 resulted in vehicle impact at 1332.63 sec into the flight. It is important to note that these errors, each taken separately, did not cause vehicle impact. Each of the trajectory errors taken separately produced a perturbed trajectory (and associated error timeline) which did not impact the Earth. One can therefore conclude that there is a region on each of the trajectory errors at parking orbit insertion which will cause vehicle impact when taken collectively, but will not cause vehicle impact when taken individually.

Case 3 yields (Table 2) the same results as the collective error condition to within 15 sec in all cases because of the smaller group of perturbations. This 15-sec error results (as in case 1) because of the 4-sec integration step size, which can cause a maximum error in the comparison tables of ±24 sec (e.g., 4 sec × 6 separate trajectories = 24 sec). This 24-sec error, however, is a random numerical one and will be 24 sec in only a few cases. Cases 4, 5, and 6 showed essentially the same results as cases 1 and 3.

Table 2 Data from perturbations[a,b]

	Case 1 and Case 3			
	Collective		Individually with superposition	
Station	ΔAOS	ΔLOS	ΔAOS	ΔLOS
BDA	0	−44	0	−34
VAN	0	−8	0	+8
CYI	−108	+84	−126	+104
TAN	−112	+260	−124	+260
CRO	+24	+200	+50	+168
WOM	+64	+208	+68	+192
CAL	+192	+144	+228	+158
WHS	+176	+136	+168	+124
CAPE	+172	+139	+168	+132
GBI	+176	+131	+164	+143
GTI	+228	+87	+226	+87
BDA	+128	+204	+130	+208
BDA	0	0	0	−8
VAN	0	+12	0	+18
CYI	−40	+40	−38	+44
TAN	−48	+108	−54	+108
CRO	−4	+108	−14	+108
WOM	+8	+112	0	+116
CAL	+76	+96	+66	+92
WHS	+76	+88	+70	+80
CAPE	+80	+92	+84	+104
GBI	+80	+92	+76	+90
GTI	+88	+91	+80	+88
BDA	+72	+112	+74	+124

[a] All time in sec.
[b] Cases 4, 5, and 6 showed essentially the same results as cases 1 and 3.

The AS-205 timeline error graphs and superposition analysis also showed that the trajectory errors which caused the most significant AOS and LOS errors, in order of decreasing importance are: flight path angle (γ), radius modulus (R), velocity modulus (v), descending node ($\mho$), and inclination angle (i) for the time interval from insertion to 9200 sec; R, γ, V, $\mho$, and i for the time interval from 9200 sec–10,500 sec; and V, R, γ, $\mho$, and i for the time interval from 10,500–16,815 sec. These conditions change, however, for a variable launch azimuth. Furthermore, the linear error regions in these trajectory variables are ±20 km in position, ±20 m/sec in velocity, ±0.5° in flight path angle, ±1.5° in inclination angle, and ±4.5° in descending node. For smaller sets of stations, the regions on these errors will increase. The variable launch azimuth does, in some cases, increase and/or decrease this range of linearity.

Sensitivity Timeline Variation as a Function of Error in Trajectory

Variables at Parking Orbit Insertion

Analysis of the AS-205 timelines showed the following behavior. Observe that these analyses relate to the 72° launch azimuth. For a variable launch azimuth the linearity ranges discussed below will increase and/or decrease. The AOS and LOS curves can also coalesce for all trajectory variables.

Perturbations in position modules only

The δR perturbations were varied from −30 km to +30 km about a nominal value of 6600.284 km. The variation in the timeline for errors in all variables was prepared from 624.63 (Parking Orbit Insertion)–16,815 sec (the end of Instrument Unit lifetime). Selected segments from 5800–6500 sec into the flight are shown in Fig. 1 (a–e).

These graphs showed slight nonlinear (considered negligible) behavior at the beginning of the mission, with complete linear behavior between 0 and ±20 km later in the flight, and with nonlinear behavior between ±20 and ±30 km for AOS and LOS times for some of the stations. The slight nonlinear behavior results from the interaction of the slower vehicle velocity at higher vehicle altitudes and the greater slant range for the greater altitude. The opposite behavior occurs for faster vehicle velocity. The velocity change due to the variation in vehicle altitude is the predominant factor which accounts for the later completely linear behavior; for an altitude increase, the velocity will decrease, which implies that the AOS and LOS times will occur later. Interacting with these later AOS and LOS times is a greater slant range which means that earlier AOS and later LOS times will result, causing the slight nonlinear behavior. The slower vehicle velocity will quickly become the predominant factor, causing the AOS and LOS times to occur later and later. The errors in the AOS and LOS times become quite large, with the LOS error being larger, ~3 hr into the flight. The opposite effect results for a negative position perturbation. Note from Fig. 1a that the slope on some AOS and LOS times, denoted by (1), is different for positive and negative values of δR. These differences in slope are attributed to the effects of the atmosphere and to the 4-sec integration step size. The small nonlinearities are denoted by (2).

Perturbations in velocity modulus only

The velocity modulus was perturbed from −50 m/sec–+50 m/sec about the nominal value of 7787.40 m/sec, and a similar timeline was prepared (Fig. 1b). This figure depicted linear behavior in AOS and LOS times from a −40 m/sec error to +40 m/sec error for all stations (except Pretoria and Tananarive, which have linearity within ±20 m/sec with

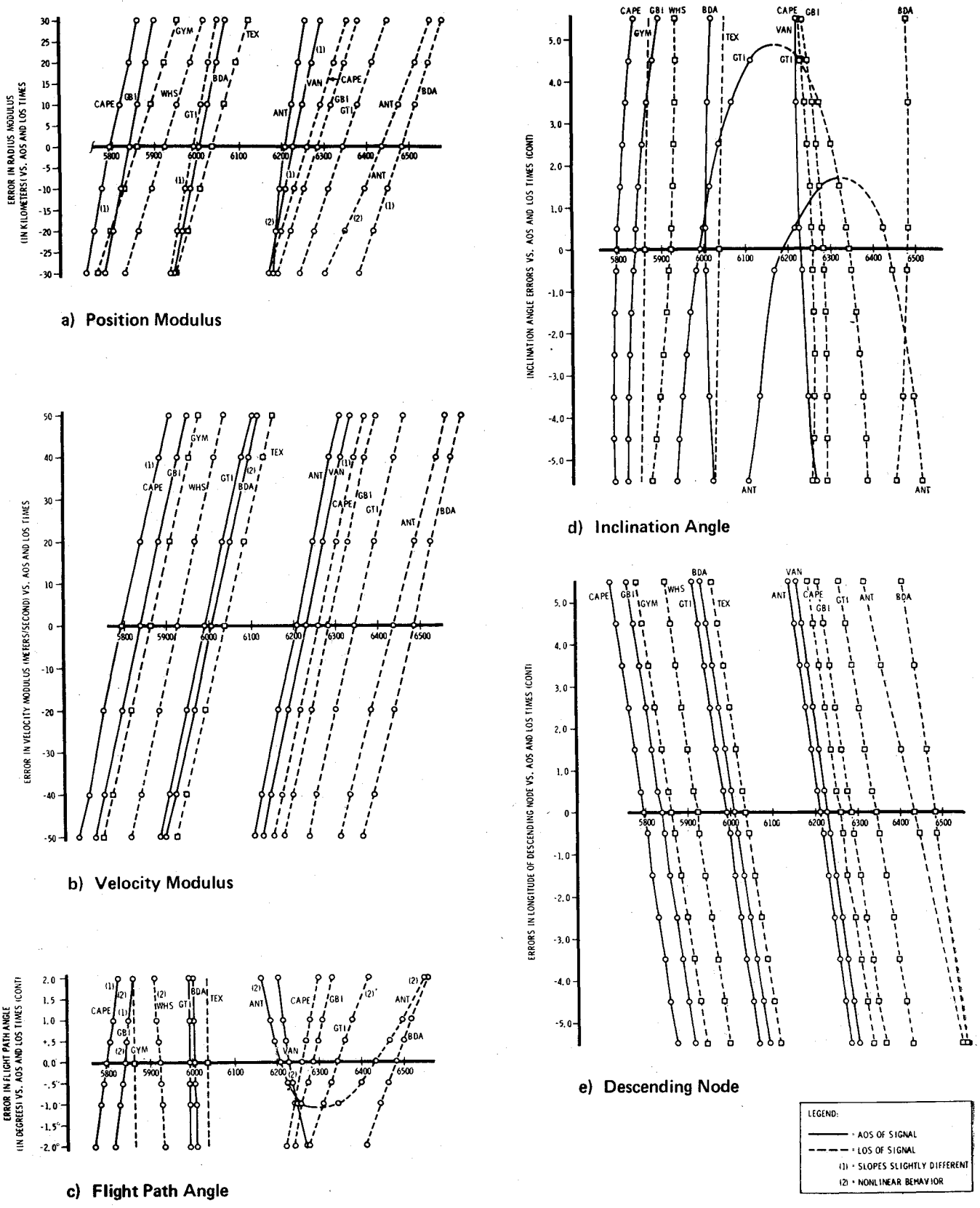

Fig. 1 Selected segments for variation in station AOS and LOS as a function of trajectory errors at parking orbit insertion.

some nonlinear behavior between ±20 and ±50 m/sec). The direction of the slopes for the velocity perturbations are in essentially the same direction as for the position perturbations at parking orbit insertion, with the larger deviations in AOS and LOS times being caused by position perturbations. (The δV at parking orbit insertion must be considered because this error results in a position perturbation through equation coupling.) A positive δV will cause a positive position oscillation above the nominal value which causes AOS to occur earlier initially and LOS to occur later. The resulting higher altitude causes the vehicle to drop behind its nominal position resulting in AOS and LOS occurring later in time as ground-lapsed time increases. The slopes on the AOS curve therefore become positive. Also observe from the timeline that the rate of change in the slopes in AOS is less than the rate of change in the LOS slopes for particular stations. The same

timeline notation applies here as described for position modulus errors.

Errors in flight-path angle only

The flight-path angle (γ) was perturbed from $-2.0°$ to $+2.0°$ (Fig. 1c) about a nominal value of 0° (actual value of 0.003°). The errors in AOS and LOS times for these perturbations exhibited linear behavior from $-0.5°$ to 0.5° for all stations with varying amounts of nonlinear behavior beyond these bounds. This nonlinear trend is attributed to the interaction of position and velocity, both of which change as a function of time in an elliptical orbit. Observe that for certain stations the AOS and LOS error curves coalesce for a γ of between $-1.0°$ to $-2.0°$. This behavior is attributed to the direction, relative to the stations, that the vehicle passes through the antenna pattern. With a $\delta\gamma$ of $+3.0°$ at parking orbit insertion, the vehicle impacted the Earth at 4152 sec into the flight with a flight path angle at impact of about $-2.0°$. This would imply that perigee for the $+3.0°$ error is considerably below the Earth's surface, and, further, that a $\delta\gamma$ of slightly greater than $+2.0°$ would also cause earth impact. Perigee for $\delta\gamma$ of $-2.0°$ at parking orbit insertion occurred 14.408 km above a spherical Earth at 1848 sec after liftoff, which would imply that a little larger negative $\delta\gamma$ would cause Earth impact. Thus, $\pm 2°$ was taken to be the upper and lower bound errors γ. These small error bounds arise from the 185.2 km nominal parking orbit altitude. A smaller numerical eccentricity will decrease the range of γ for vehicle impact. This was the case for the AS-503 sensitivity simulation analysis results.

Perturbations in inclination angle only

The inclination angle was perturbed from $-5.5°$ to $+5.5°$ about a nominal value of 31.605° and a graph of perturbation vs AOS and LOS times was constructed (Fig. 1d). This graph showed slight nonlinearity in AOS and LOS times; however, between $-2.5°$ and $+2.5°$, a straight-line approximation introduces an error of $\sim$10 sec in the worst case, but, in most cases, no more than 5 sec, depending upon the particular station. Between $-1.5°$ and $+1.5°$ no nonlinearity can be detected graphically. Strong nonlinearity occurs only where the AOS and LOS curves for a particular station coalesce. This occurs when the perturbation causes the trajectory barely to cross the coverage circle of the station. This occurs in only three instances between 624.63 sec and 16,815.8 sec, and it occurs outside the $\delta i = \pm 2.5°$ range. For 75% of the stations, a straight-line approximation from $-5.5°$ to $+5.5°$ introduces an error of approximately 10 to 15 sec, which for the purpose of AOS and LOS, is insignificant.

Perturbations in descending node only

The descending node was perturbed from $-5.5°$ to $+5.5°$ about a nominal value of 119° with respect to the launch meridian, or 38.4407° with respect to the Greenwich meridian, and a graph of perturbations vs AOS and LOS times was constructed (Fig. 1e). These curves showed definite linear behavior between $-4.5°$ to $+4.5°$. For a few stations, small nonlinear behavior is detected when the curves are extended to $\pm 5.5°$. A straight-line approximation produces δt of 20 sec in the worst case; in most cases, the error from such an approximation is approximately 5–10 sec.

The linear behavior arises from the manner of movement of the trajectory across a station coverage circle due to perturbations in $\mathfrak{V}$. This relationship becomes nonlinear when the AOS and LOS curves coalesce, corresponding to the movement of the trajectory from across a coverage circle to outside the circle.

Variation in parking orbit insertion time

The nominal trajectories were simulated for AS-205 parking orbit insertion times of 603.63 and 624.63 sec, respectively. Perturbation curves for t_i = 603.63 sec were developed to the end of passivation and compared to the perturbation curves for t_i = 624.63 sec. The difference in AOS and LOS times varied from about 5–10 sec for the nominal simulation and perturbed simulation of $\delta R = \pm 25$km, $\delta V = \pm 25$ m/sec, and $\delta\gamma = +1.0°$. The variation in AOS and LOS times for the nominal and for errors of $\pm 5.5°$ in the inclination angle and descending node was about 5–7 sec.

These results show that the changes in AOS and LOS are less than the change in ascent-to-orbit time. See also Table 3, which shows the same results for the AS-503 and AS-504 missions. This condition results because the ascent-to-orbit trajectory trace cannot be directly added to the parking orbit trajectory trace, relative to AOS and LOS times.

AS-205 Postflight Evaluation Analysis

The AS-205 preflight and LVDC postflight data showed that the deviations from the nominal insertion state were small. The parking orbit insertion time error will produce about a 1-sec error (AOS and LOS 1 sec later), while the errors in γ, i, and $\mathfrak{V}$ will produce negligible AOS and LOS errors. The error in radius modulus will cause AOS and LOS to occur 1 sec later. The error in V will produce about a 1-sec error in AOS and LOS out to about 2200 sec with a 5–10-sec maximum AOS and LOS error from 2200–13600 sec (occurring for the most part in later AOS and LOS times). From 13,600 to 16,800 sec, the error in the AOS and LOS times occurred 10–15 sec later. It is therefore concluded that the trajectory and parking orbit insertion time errors will produce negligible effects on the nominal AOS and LOS times.

Sensitivity AOS and LOS times and available post-flight AOS and LOS times as obtained from the real-time network and Post-Launch Instrumentation Message (PLIM) radar data show agreement to within 30 sec in the majority of the cases. The 30-sec difference is essentially a measure of the difference between the sensitivities nominal and the real-time network data that is subject to refractive bending.

AS-503 Sensitivity and Postflight Data Analysis

Sensitivities Timeline Error Graph Preparation for AS-503

The approach is essentially the same as that used in the preparation of the 205 sensitivity graphs, except that a variable flight azimuth and more stations were used. The behavior of the nominal and perturbed coverage times and of the nominal and perturbed AOS and LOS, as functions of a fixed flight azimuth for a continuous range of trajectory errors at parking orbit insertion, has been described. How-

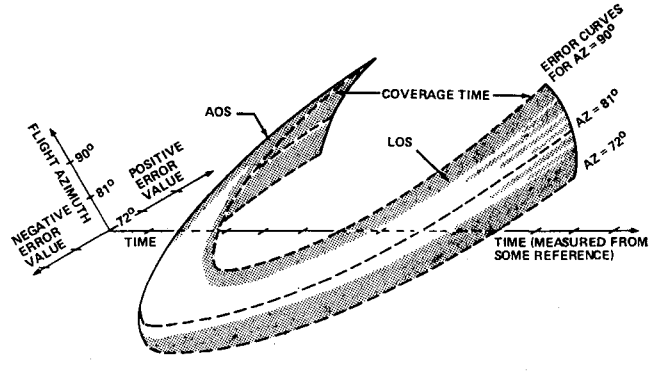

Fig. 2 Three-dimensional representative sensitivites graph for one station.

Table 3 Comparison of AS-503 sensitivities nominal results and AS-504 nominal data

For zero degrees elevation angle					
AS-503 Sensitivities data AZ = 72°			AS-504 Data		
Station	AOS	LOS	AOS	LOS	
CYI	16:35	23:29	16:27	23:35	
TAN	16:59	42:36	36:57	42:35	1st orbital phase
CRO	52:21	58:14	52:07	58:08	
CNB (HSK)	59:32	1:05:40	59:25	1:05:40	
HTV			1:08:08	1:12:06	
RED			1:19:04	1:24:57	
CAL	1:28:19	1:32:35	1:28:17	1:32:48	
GYM	1:28:12	1:35:16	1:28:14	1:35:28	
WHS			1:29:42	1:36:36	
GDS	1:28:50	1:33:40	1:28:54	1:33:47	
TEX	1:31:08	1:38:02	1:31:08	1:38:20	
MIL	1:34:53	1:41:55	1:35:02	1:42:03	
GBI	1:35:48	1:42:11	1:35:45	1:42:24	
BDA	1:38:27	1:45:33	1:38:28	1:45:46	
VAN	1:42:36	1:49:15	1:42:48	1:49:55	
CYI	1:50:03	1:55:23	1:50:05	1:55:32	2nd orbital phase
CRO	2:50:35	2:31:59	2:25:23	2:31:56	
HAW	2:50:35	2:56:36	2:50:45	2:57:00	
RED			2:52:34	2:58:32	
GDS	3:00:09	3:07:07	3:00:34	3:07:32	
GYM	3:01:15	3:08:11	3:01:28	3:08:36	
TEX	3:04:27[a]	3:11:07	3:04:36	3:11:33	
MIL	3:08:03	3:15:07	3:08:20	3:15:30	
GBI	3:08:51	3:15:39	3:09:04	3:16:01	
GTK			3:11:30	3:17:30	3rd orbital phase
BDA	3:11:23	3:18:19	3:11:38	3:18:40	
ANT	3:14:11	3:19:15	3:14:24	3:19:44	
ASC	3:27:55	3:33:23	3:28:11	3:33:56	
PRE			3:38:56	3:45:58	
TAN	3:43:23	3:48:13	3:43:43	3:48:31	
CRO	3:58:13	4:04:59	3:58:21	4:05:34	
HTV			4:14:51	4:17:43	
HAW	4:22:51	4:29:55	4:23:14	4:30:29	

[a] 3:04:27 is read as 3 hr 4 min and 27 sec ground-elapsed time.

ever, additional analysis methods are required because of the variable flight azimuth. The sensitivities analyses were formulated for the individual azimuth angles 72, 81, 90, 99, and 108°. Figure 2 depicts an example of the behavior of AOS and LOS and coverage times for errors at Tananarive, and certain other stations. To read the graphs easily, the AOS and LOS surfaces were projected on the time-error plane as a series of concentric curves as a function of the specified azimuth angles. There are five separate errors at parking orbit insertion (see Mathematical Appendix) and two sets of sensitivities graphs; one for each azimuth range set (72°–90° and 90°–108°); therefore, ten separate graphs are required. The flight azimuth dictates which set of graphs is to be used. The AOS and LOS for the reconfigured network is obtained by the algebraic addition of the separate AOS and LOS deviations from the nominal. For any flight azimuth not specifically mapped on the time-error plane, the AOS and LOS error curves may be inserted by using the nominal AOS and LOS times for that azimuth and the general shape of the error curves bounding that azimuth. These graphs (not included here) are similar to and more complicated than the graphs of Fig. 1.

These graphs were prepared, using the injection to plumbline analysis discussed in the Appendix in conjunction with trajectory and AOS and LOS simulation techniques. The individual trajectory errors and range of trajectory errors at parking orbit insertion considered for the 72° flight azimuth have been discussed. The range, however, for γ is $\pm 1.5°$ because the AS-503 parking orbit has a smaller numerical eccentricity.

The resulting graphs are not restricted to the parking orbit of the Apollo 8 mission but are applicable to other Apollo missions, because: 1) the geometry of the stations with respect to the launch meridian is fixed, 2) the same type of launch vehicle is used, and 3) the abscissa was initiated at time base 5(S-IVB engine cutoff) plus 9.8 sec. These graphs may be used for other Apollo missions as shown in Table 3, which is a comparison of the AOS and LOS times of the AS-503 parking orbit data (for the 72° flight azimuth) vs the AS-504 data, which also had a 72° flight azimuth. Observe the close agreement. The parking orbit insertion times for these data were 691 and 649 sec, respectively.

The trajectory analysis also showed that a region of trajectory errors exists at parking orbit insertion which, if exceeded, will cause vehicle impact when taken individually. The most significant error here is the flight-path angle error coupled with the orbital numerical eccentricity.

Apollo 8 Real-Time and Postflight Data Analysis

Hard copy trajectory data in the new plumbline (see Appendix) system was obtained at the ground-elapsed times, 776, 784, 790, 907, and 1027 sec. Teletype floating point octal trajectory data in the ephemeral (Apollo 4) system were also obtained from Houston at the ground-elapsed times, 889, 5454, and 6689 sec.

These data were converted to the required errors at parking orbit insertion by the methods outlined in the Appendix. An analysis of the trajectory data, the errors at the time of the transmitted trajectory data, and the resulting propagated errors at parking orbit insertion were developed using the methods described in the Appendix. The results showed that the actual parking orbit insertion errors are small, and that the propagation procedure yields accurate results using trajectory data in the region immediately past parking orbit insertion. Table 4 depicts the AOS and LOS times as obtained from the network, from the sensitivities, and from three verification simulation runs. These simulation runs used the real-time transmitted new plumbline data at the ground-elapsed times, 776, 790, and 1027 sec, as inputs. Observe that the actual data, sensitivities results, and simulation verification runs agree very closely in the AOS and LOS times for all stations. Note also the effects of refractive

Table 4 Comparison of actual data, sensitivities results, and simulation results for the AS-503 (Apollo 8) mission

	Actual		Sensitivities		Simulation run 1 GET[a] = 776 sec		Simulation run 2 GET = 790 sec		Simulation run 3 GET = 1027 sec	
Station	AOS	LOS	AOS	LOS	AOS	LOS	AOS	LOS	AOS	LOS
BDA	...	13:15[b]	...	12:43	...	13:04	...	...	...	...
VAN	...	16:12	...	15:32	...	15:52	...	15:50	...	...
CYI	16:25	24:02	16:35	23:39	16:48	24:00	16:54	23:58	...	23:55
TAN	36:58	42:45	36:59	42:36	37:20	42:56	37:18	42:54	37:15	42:59
CRO	51:45	58:38	52:21	58:14	52:32	58:24	52:38	58:22	52:35	58:27
HSK	1:00:32	1:05:46	59:32	1:05:40	59:52	1:06:00	59:50	1:05:58	59:47	1:05:55

[a] GET—Ground elapsed time of state vector used in analysis.
[b] Data is read as 1:38:41 = 1 hr, 38 min, 41 sec.

bending (see below) by comparison of the actual vs the sensitivities data. Because Apollo 8 attained so nearly a perfect insertion state, the sensitivity nominal results, adjusted to ground-elapsed time, were used for network configuration.

Summary of Results of Theoretical vs Actual Network Coverage for AS-204 and AS-501 Missions

What follows is a summary of the results for the AS-204 and AS-501 missions, which are discussed in Ref. 1. This reference considered the subjects, which are discussed in the following paragraphs: 1) refractive bending of RF signals, 2) multipath, 3) signal dropout, and 4) polarization diversity.

The refractive bending analysis demonstrated that refractive bending contributes to reception of the RF signal by a ground station before a vehicle reaches the horizon and after a vehicle has disappeared over the horizon. The result of this effect is reliable communications at lower elevation angles than previously anticipated. Reliable reception of the RF signal from 0–0° elevation was demonstrated by the AS-204 and AS-501 flights. The sensitivity timeline error graphs were therefore prepared using the 0° elevation angle. A secondary effect of refractive bending is that early acquisition of the RF signal causes sidelobe tracking by the ground stations. This situation results in a weak RF signal and more frequency dropouts.

The multipath study determines the minimum elevation angle at which reliable communications are practical. The data from the AS-204 and AS-501 flights demonstrated that reliable communication is generally possible from 0° elevation to 0° elevation for both CCS and VHF systems while the vehicle is in low Earth orbit. The refractive bending contributes to communications reliability at these lower elevation angles by making the elevation angle in the direction from which the RF signal emanates greater than the actual elevation angle from ground station to vehicle, thus minimizing the scattering effects of the Earth's surface.

The signal dropout analysis determined the causes of RF signal dropout. It was concluded that RF signal dropouts are caused by multipath effects, vehicle antenna nulls, attenuation due to flame and venting, and ground station errors. The proper use of preflight predictions (including all updates at the ground stations just prior to a pass) can aid acquisition procedures, especially if these predictions include the refractive bending effects. Assuming the ground station receiving antenna is pointed toward the horizon of the oncoming vehicle at the proper azimuth, a delay of approximately 15 sec from the time the signal is first received until the antenna begins to track in the program track mode could reduce the possibility of a sidelobe tracking and the resulting problems. This delay would compensate for the initial pointing error due to refractive bending.

The polarization diversity study ascertained the value of polarization diversity through use of multiple antennas at the ground stations. It was concluded that there were instances where the signal being received in one polarization mode dropped below threshold while the signal received in the other mode did not. Thus, where a critical need for the telemetry data exists, polarization diversity increased the reliability of receiving that data.

Conclusions

The sensitivities analysis, associated trajectory analysis, and simulation results showed the following important conclusions.

1) The changes in AOS and LOS times are approximately linear for the following range of trajectory errors at parking orbit insertion: ±20 km in position modulus, ±20 m/sec in velocity modulus, ±0.5° in flight-path angle, ±1.5° in inclination angle, and ±4.5° in descending node. For a large number of stations, the change in the AOS and LOS times is linear for a larger range of these trajectory errors. The variable flight azimuth does, in some cases, increase and/or decrease this range of linearity.

2) The superposition principle generally yields network timeline results to within 15 sec for the positive and negative trajectory perturbations studies, when compared to the timelines for these perturbations taken collectively.

3) The superposition principle also yields acceptable results for magnitudes of trajectory errors which produce nonlinear changes in the AOS and LOS times. Although the AOS and LOS are nonlinear functions of the trajectory errors, the nonlinearity is weak, and a linear approximation is feasible.

4) There exists a region of trajectory errors at parking orbit insertions which, if exceeded, will cause vehicle impact when taken individually. The most significant error here is the flight path angle error coupled with the orbital numerical eccentricity.

5) For the Apollo 8 mission the AOS and LOS times obtained from the network, the sensitivities, and the simulation verification runs agree to within 15 sec for the majority of the stations.

6) The sensitivities timeline error graphs prepared for the Apollo 8 variable flight azimuth may also be used for other Saturn missions.

7) Comparison of the sensitivities analysis results and available real-time network data for the AS-205 mission shows agreement to within 30 sec in the majority of the cases. This 30-sec error arises primarily from the effects of refractive bending and multipath.

Appendix

Contained herein are the development of the forward and backward transition matrices, injection to plumbline analysis, ephemeral propagation analysis, new plumbline propagation analysis, and orientation of the ephemeral to the launch meridian analysis. Because the general methods used to obtain transition matrices are well known, only an outline of the solution for the forward transition matrix will be discussed here. The perturbation equations for a centrobaric field were first obtained and then linearized. Then this linear differential system was specialized to the circular orbit by assuming both the radius modulus (R) and the angular velocity ($\omega = \dot{\theta}$) to be constant. These assumptions transform the linear differential system into one with constant coefficients which can then be easily integrated. Also the Saturn V parking orbits are those of small numerical eccentricity. This system was then integrated and the constants

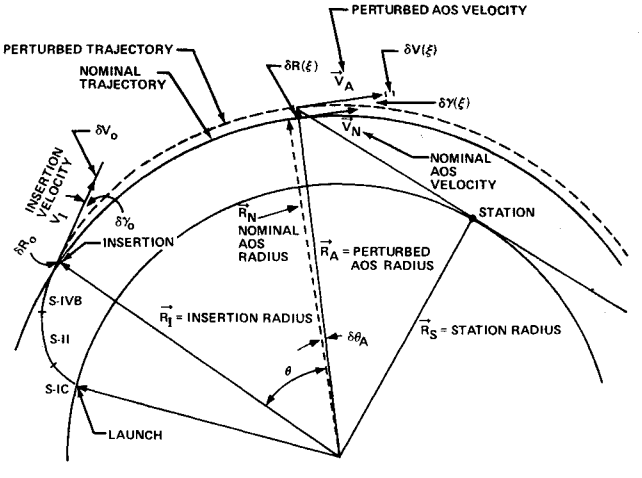

Fig. 3 Planar view (not to scale) of transition matrix geometry related to station AOS.

of integration evaluated using the initial conditions. Additional manipulation to transform the δR, $\delta \dot{R}$, $\delta\theta$ and $\delta\dot{\theta}$ variables into those of Fig. 3 (δR, $\delta\theta$, δV, and $\delta\gamma$) were then executed so as to obtain the transition matrix in the following form:

$$\begin{bmatrix} \delta R \\ \delta\theta \\ \delta V \\ \delta\gamma \end{bmatrix} = \begin{bmatrix} [2 - c(\omega t)] & 0 & 2\frac{R}{V}[1 - c(\omega t)] \\ \frac{1}{R}[2s(\omega t) - 3\omega t] & 1 & +\frac{1}{V}[4s(\omega t) - 3\omega t] \\ \frac{V}{R}[c(\omega t) - 1] & 0 & [2c(\omega t) - 1] \\ \frac{1}{R}s(\omega t) & 0 & \frac{2}{V}s(\omega t) \end{bmatrix} \times \begin{bmatrix} Rs(\omega t) \\ \{2[c(\omega t)] - 1\} \\ -V[s(\omega t)] \\ s(\omega t) \end{bmatrix} \times \begin{bmatrix} \delta R_0 \\ \delta\theta_0 \\ \delta V_0 \\ \delta\gamma_0 \end{bmatrix} \quad \text{(A1)}$$

where $s = \sin$, $c = \cos$.

In Eq. (A1) the subscript 0 on the right side of the equation depicts the errors at parking orbit insertion while the errors on the left side are those resulting after some elapsed time (Fig. 3). The constant angular rate ω is given by $\omega = (\mu e/R^3)^{1/2}$ where $\mu_e = 3.986032 \times 10^5\ \text{km}^3/\text{sec}^2$, R = nominal radius at parking orbit insertion, and V = nominal velocity at parking orbit insertion.

Note from Eq. (A1) that there are four variables at parking orbit insertion, but Fig. 3 depicts only three variables. This condition results because the Iterative Guidance Mode (IGM) in the Saturn system is an implementation of the range-free optimal steering law obtained from the flat-free optimal steering law obtained from the flat-Earth equations using the calculus-of-variations. The flat-Earth equations

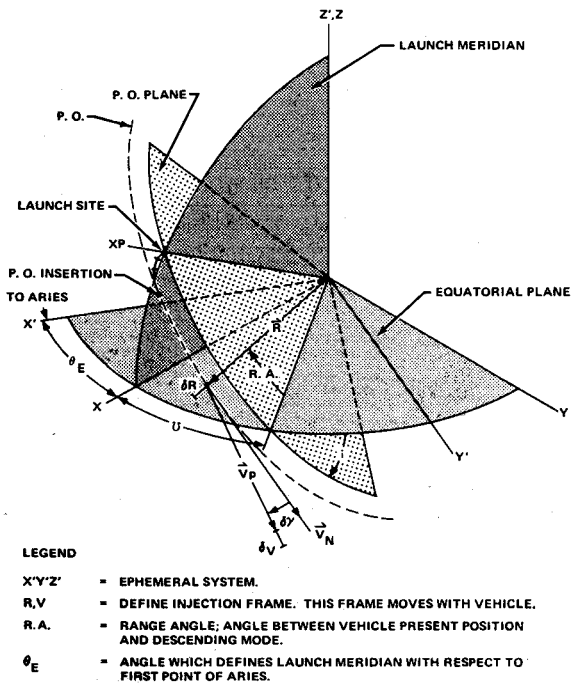

Fig. 4 Geometry between injection, ephemeral, and plumbline coordinate frames.

are formulated as a problem of Mayer and the general bilinear steering law is obtained using the Euler-Lagrange equations. This general steering law is then specialized, using the transversality conditions, for the boundary value problems of, a) range free and attitude free and b) range free only. The first boundary value problem yields the constant steering law ($\tilde{\chi}$) while the second boundary value problem yields the linear-tangent steering law

$$\tan\chi = (E/D)t + E/D \quad \text{(A2)}$$

which is expanded into a linear form in χ (because of the actual behavior of $\tan\chi$) to obtain

$$\chi \doteq E/D - B/Dt \quad \text{(A3)}$$

This result is combined with boundary value problem a so that the constraint equations can be integrated subject to Eq. (A3) to obtain

$$\chi_j = \tilde{\chi}_j - K_i + K_m t \quad \text{(A4)}$$

where K_i, K_m, χ_j result using the IGM equations. Because altitude is specified (boundary problem b), the optimal steering equations in both the pitch and yaw planes are an implementation of the range-free problem. This analysis may be found in detailed development in Ref. 2, pages VI-1–VI-57. Because of the range-free problem, it follows that $\delta\theta_0 = 0$.

Formulation of Backward Transition Matrix

The purpose of this analysis is to develop the procedure which will allow propagation of the in-plane errors δR_ξ, δV_ξ, and $\delta\gamma_\xi$ back to parking orbit insertion (Fig. 3). Observe from Fig. 3 that there is also an in-plane error $\delta\theta_\xi$. This error is not projected back to parking orbit insertion because IGM is a range-free guidance scheme, which means that there is no constraint on the downrange angle. These in-plane errors may be projected back to either changing the sign in $(t_\xi - t_I)$ of Eq. (A1), or by using the method of adjoints. Using $t' = -t$ the circular functions of Eq. (A1) become

$$\cos(-\omega t) = \cos(\omega t'),\ \sin(-\omega t) = -\sin(\omega t') \quad \text{(A5)}$$

Substituting Eq. (A5) into Eq. (A1) yields

$$\begin{bmatrix} \delta R_0 \\ \delta\theta_0 \\ \delta V_0 \\ \delta\gamma_0 \end{bmatrix} = \begin{bmatrix} 2 - c(\omega t') & 0 & 2\frac{R}{V}[1 - c(\omega t')] \\ \frac{1}{R}[-2s(\omega t') + 3\omega t'] & 1 & -\frac{1}{V}4[s(\omega t') + 3\omega t'] \\ \frac{V}{R}[c(\omega t') - 1] & 0 & [2c(\omega t') - 1] \\ -\frac{1}{R}s(\omega t') & 0 & -\frac{2}{V}s(\omega t') \end{bmatrix} \times \begin{bmatrix} [Rs(\omega t')] \\ 2[c(\omega t') - 1] \\ +Vs(\omega t') \\ c(\omega t') \end{bmatrix} \times \begin{bmatrix} \delta R_\xi \\ \delta\theta_\xi \\ \delta V_\xi \\ \delta\gamma_\xi \end{bmatrix} \quad \text{(A6)}$$

where $s = \sin$; $c = \cos$. Equation (A6) is the propagation equation which projects the in-plane errors at time (t_ξ) back to parking orbit insertion. Note that the errors in inclination angle and descending node (Fig. 4) define the change in orientation of the nominal parking orbit plane and as such are constant except for effects of nutation in the inclination angle and the precession of the descending node, both due to earth oblate-

ness. The precession must be considered if $t' = (t_I - t_\xi)$ is sufficiently large. The R and V are the nominal values at the time t_ξ, as obtained using a simulation which included the effects of earth oblateness and drag. Figure 4 describes the geometry of the coordinate frames used for the injection to plumbline analysis. This particular analysis is required to ensure that the errors comprising the sensitivity graphs are only those errors which are depicted on the ordinates of Fig. 1. For this particular analysis the injection frame is frozen at parking orbit (PO) insertion. The first step is to express the components in the injection frame due to the δR, δV, and $\delta\gamma$ errors.

$$\dot{\mathbf{X}}_V = \begin{bmatrix} X_{VP} \\ Y_{VP} \\ Z_{VP} \end{bmatrix} = \begin{bmatrix} R_N + \delta R \\ 0 \\ 0 \end{bmatrix} \tag{A7}$$

and

$$\dot{\mathbf{X}}_V = \begin{bmatrix} \dot{X}_{VP} \\ \dot{Y}_{VP} \\ \dot{Z}_{VP} \end{bmatrix} = \begin{bmatrix} (V_N + \delta V)\sin(\gamma_N + \delta\gamma) \\ 0 \\ (V_N + \delta V)\cos(\gamma_N + \delta\gamma) \end{bmatrix} \tag{A8}$$

The transformation from the injection to the new plumbline (Apollo 13) systems is given by

$$\begin{aligned} \mathbf{X}_P &= \{[\mathrm{AP}]^T x [\mathrm{R.A.}]^T\} x \mathbf{X}_V \\ \dot{\mathbf{X}}_p &= \{[\mathrm{AP}]^T x [\mathrm{R.A.}]^T\} x \dot{\mathbf{X}}_V \end{aligned} \tag{A9}$$

Here [AP] is the matrix transform from the new plumbline to the space-fixed orthogonal system with the X axis through the descending node (target frame) and [R.A.] is the matrix transform from the target to the injection frame.

The [AP] matrix involves the azimuth angle, launch latitude, inclination angle, and descending node. Therefore, Eqs. (A7–A9) may be used to uniquely define the vehicle components of state, in the plumbline system, for any individual or combination of errors in the radius modulus, velocity modulus, flight-path angle, inclination angle, and descending node. This analysis was used to obtain the initial components of state and experimentally verify (in conjunction with trajectory simulation) the superposition principle as applied to the sensitivity graphs and analysis.

Ephemeral Propagation Analysis

Because real-time trajectory data are obtained from Houston in Ephemeral System, a method must be developed to express the trajectory errors in δR, δV, $\delta\gamma$, δi, and $\delta\mho$ at parking orbit insertion in terms of this data. This procedure is formulated as follows. The transformation from the Ephemeral System to the XYZ System (see Fig. 4) follows as

$$\begin{bmatrix} \dot{X} \\ \dot{Y} \\ \dot{Z} \end{bmatrix}\begin{bmatrix} X \\ Y \\ Z \end{bmatrix} = \begin{bmatrix} \cos\theta_E & \sin\theta_E & 0 \\ -\sin\theta_E & \cos\theta_E & 0 \\ 0 & 0 & 1 \end{bmatrix} \times \begin{bmatrix} X \\ Y \\ Z \end{bmatrix}' \begin{bmatrix} \dot{X} \\ \dot{Y} \\ \dot{Z} \end{bmatrix}' \tag{A10}$$

Where $\theta_E = \theta_{EO} + \omega_e(T_L - T_{LO})$; T_{LO} = nominal launch time; T_L = actual launch time; θ_{EO} = nominal value of θ_E; ω_e = 15.048 deg/hr (Earth rotational rate).

The perturbed radius modulus, velocity modulus, and flight-path angle at the time trajectory data are transmitted (t_ξ) follow from

$$\begin{aligned} &R_P = (X^2 + Y^2 + Z^2)^{1/2}; \quad V_P = (\dot{X}^2 + \dot{Y}^2 + \dot{Z}^2)^{1/2} \\ &\gamma_P = \sin^{-1}(P_1/R_P V_P), \text{ and } P1 = X\dot{X} + Y\dot{Y} + Z\dot{Z} \end{aligned} \tag{A11}$$

The perturbed values of inclination angle and descending node are given by

$$i_p = \cos^{-1}(L_Z/L), \ \mho_p = \tan^{-1}(L_X/L_Y) + 180^\circ \tag{A12}$$

where $L_X = Y\dot{Z} - Z\dot{Y}$; $L_Y = Z\dot{X} - XZ$; $L_Z = X\dot{Y} - Y\dot{X}$, and $L = (L_X^2 + L_Y^2 + L_Z^2)^{1/2}$. The errors in these variables at t_ξ therefore follow directly from

$$\begin{aligned} &\delta R = R_P - R_N; \ \delta V = V_P - V_N; \ \delta\gamma = \gamma_P - \gamma_N \\ &\delta i = i_p - i_N, \text{ and } \delta\mho = \mho_p - \mho_N \end{aligned} \tag{A13}$$

These δR, δV, etc. variables include the effects of oblateness and drag, because R_P, R_N, V_P, V_N, etc. contain these effects.

The transition matrix equations previously discussed may be used to transform these errors back to parking orbit insertion; that is, the adjoint system defines the errors at parking orbit insertion which caused the errors of Eq. (A13).

New Plumbline Propagation Analysis

Hard copy data of the real-time trajectory is also available from HOSC (display number SP-104) in the new plumbline system. This data must also be transformed to obtain the trajectory errors at parking orbit insertion. The first step in this analysis is to transform from the new plumbline to the XYZ System (Fig. 4). This transformation is given by

$$\begin{bmatrix} \dot{X} \\ \dot{Y} \\ \dot{Z} \end{bmatrix}; \begin{bmatrix} X \\ Y \\ Z \end{bmatrix} = \begin{bmatrix} P_1 & P_2 & P_3 \\ P_4 & P_5 & P_6 \\ P_7 & P_8 & P_9 \end{bmatrix} \times \begin{bmatrix} X_P \\ Y_P \\ Z_P \end{bmatrix}; \begin{bmatrix} \dot{X}_P \\ \dot{Y}_P \\ \dot{Z}_P \end{bmatrix} \tag{A14}$$

where $P_1 = \cos(\phi)$, $P_2 = \sin(\phi)\sin(AZ)$, $P_3 = \sin(\phi)\cos(AZ)$, $P_4 = 0$, $P_5 = \cos(AZ)$, $P_6 = \sin(AZ)$, $P_7 = \sin(\phi)$, $P_8 = -\cos(\phi)\sin(AZ)$, $P_9 = \cos(\phi)\cos(AZ)$, and ϕ = launch geodetic latitude, and AZ = flight azimuth. The trajectory errors at t_ξ follow from Eqs. (A11–A13). These errors are then projected back to parking orbit insertion using the transition matrix previously described.

References

[1] "Atmospheric Refraction and Tracking Prediction Technique," New Technology Report, 68-266-0047, IBM; also MSFC III-6-137, Reportable Item 14000-133, NASA; originators W. H. Land Jr. and N. K. Denmark.

[2] "Phase I Systems Recommendation Document," MSFC III-4-4434-I, NASA; also 65-228-0001H, IBM.